Review of Scientific Instruments ARTICLE scitation.org/journal/rsi

Flight demonstration of a miniature atomic scalar magnetometer based on a microfabricated rubidium vapor cell

Cite as: Rev. Sci. Instrum. 94, 035002 (2023); doi: 10.1063/5.0135372
Submitted: 18 November 2022 • Accepted: 7 February 2023 •
Published Online: 3 March 2023

View Online Export Citation CrossMark

Haje Korth,[1,a)] John E. Kitching,[2] John W. Bonnell,[3] Brian A. Bryce,[1] George B. Clark,[1] Weston K. Edens,[1] Christopher B. Gardner,[1] William Rachelson,[3] and Amanda Slagle[3]

AFFILIATIONS

[1] The Johns Hopkins University Applied Physics Laboratory, Laurel, Maryland 20723, USA
[2] National Institute of Standards and Technology, Boulder, Colorado 80305, USA
[3] Space Sciences Laboratory, University of California, Berkeley, California 94720, USA

[a)] **Author to whom correspondence should be addressed:** haje.korth@jhuapl.edu

ABSTRACT

We have developed an atomic magnetometer based on the rubidium isotope ^{87}Rb and a microfabricated silicon/glass vapor cell for the purpose of qualifying the instrument for space flight during a ride-along opportunity on a sounding rocket. The instrument consists of two scalar magnetic field sensors mounted at 45° angle to avoid measurement dead zones, and the electronics consist of a low-voltage power supply, an analog interface, and a digital controller. The instrument was launched into the Earth's northern cusp from Andøya, Norway on December 8, 2018 on the low-flying rocket of the dual-rocket Twin Rockets to Investigate Cusp Electrodynamics 2 mission. The magnetometer was operated without interruption during the science phase of the mission, and the acquired data were compared favorably with those from the science magnetometer and the model of the International Geophysical Reference Field to within an approximate fixed offset of about 550 nT. Residuals with respect to these data sources are plausibly attributed to offsets resulting from rocket contamination fields and electronic phase shifts. These offsets can be readily mitigated and/or calibrated for a future flight experiment so that the demonstration of this absolute-measuring magnetometer was entirely successful from the perspective of increasing the technological readiness for space flight.

© 2023 Author(s). All article content, except where otherwise noted, is licensed under a Creative Commons Attribution (CC BY) license (http://creativecommons.org/licenses/by/4.0/). https://doi.org/10.1063/5.0135372

I. INTRODUCTION

High-accuracy magnetic field measurements are important for many scientific missions in the near-Earth space environment and beyond for planetary exploration (Acuña, 2002, and references therein). Reference magnetometers based on atomic standards have proven to be highly accurate and had their debut in space many decades ago (Ness *et al.*, 1961). The advent of small-scale atomic sensor technology (Kitching, 2018), which is capable of measuring the magnetic field absolutely yet requires few mass and power resources, puts ubiquitous use of high-accuracy magnetic field measurements within reach. One such instrument is an optically pumped, atomic magnetometer based on the rubidium isotope ^{87}Rb developed in collaboration between the Johns Hopkins University Applied Physics Laboratory, the Johns Hopkins University Whiting School of Engineering, and the National Institute of Standards and Technology (Korth *et al.*, 2016a). The capability of this instrument to survive and operate under environmental conditions encountered during space flight has now been tested and demonstrated during a flight on a sounding rocket within the Twin Rockets to Investigate Cusp Electrodynamics 2 (TRICE-2) mission.

The scientific goal of the TRICE-2 dual-rocket campaign was to observe the spatial and temporal behavior of ion precipitation and electrodynamics in the Earth's northern cusp region in order to determine whether any dynamic structures are the result of temporal or spatial variation in magnetopause reconnection. To accomplish this goal, a pair of almost identically instrumented scientific payloads was launched on December 8, 2018 from Andøya, Norway along similar ground tracks but at different apogee altitudes (750 km for low flyer and 1200 km for high flyer) into the

Downloaded from http://pubs.aip.org/aip/rsi/article-pdf/doi/10.1063/5.0135372/16798194/035002_1_online.pdf

© Author(s) 2023

Earth's cusp region during a period when optical data showed the presence of poleward-moving auroral forms and radar data indicated that significant ionospheric signatures of reconnection are present. In addition to the scientific payload, the low-flying sounding rocket carried our atomic magnetometer for demonstration purposes.

In this paper, we first describe the flight model Miniature Absolute Scalar Magnetometer (MASM) with a focus on hardware revisions with respect to the prior-generation instrument in Sec. II. We then present the rocket trajectory and the measurements acquired during the campaign in Sec. III. The flight model instrument was subjected to limited testing prior to launch. Therefore, in Sec. IV, we provide complementary laboratory measurements using the engineering model instrument conducted post-launch to validate the performance of the instrument. In Sec. V, we discuss the observations in the context of the space and rocket environment in which they were acquired. Finally, the results and development status of the magnetometer are summarized in Sec. VI.

II. FLIGHT HARDWARE

The instrument advanced for space flight is an atomic magnetometer (Budker and Jackson Kimball, 2013) based on the rubidium isotope ^{87}Rb developed and described by Korth *et al.* (2016a). Atomic magnetometers infer the scalar magnetic field from the Larmor precession of atomic spins, whereby the associated Larmor frequency, f[Hz] = $\gamma B/2\pi$, is proportional to B and the gyromagnetic ratio, $\gamma/2\pi$. For ^{87}Rb, the gyromagnetic ratio is $\gamma/2\pi \cong 7$ Hz/nT. The operating principle is such that a cell containing the alkali-metal vapor is illuminated with circularly polarized light with a wavelength that corresponds to resonance with an optical (electronic) transition in the atoms. Under these conditions, atoms are optically pumped into a nonthermal population distribution, and the vapor cell becomes more transparent to the optical beam. A radio frequency (RF) signal is then applied at the Larmor precession frequency to excite an oscillating coherence within the atoms, which causes a time-dependent modulation of the optical transmission. By detecting the phase shift of the optical modulation with respect to the stimulus, the Larmor frequency, and, therefore, the magnetic field magnitude, can be determined.

The sensor technology is based on a low-power semiconductor laser (vertical-cavity surface-emitting laser or VCSEL) and a miniature rubidium vapor cell of millimeter dimensions produced using modern microfabrication processes (Liew *et al.*, 2004; 2007). Based on a microelectromechanical system (MEMS) design, these vapor cells have been used as frequency references in atomic clocks (Knappe *et al.*, 2004), but they also have been shown to function as sensitive magnetometers (Schwindt *et al.*, 2004; 2007). The combination of a MEMS vapor cell and a VCSEL has allowed a substantial reduction in mass, size, and power consumption of both clocks (Mescher *et al.*, 2005) and magnetometers (Mhaskar *et al.*, 2012).

The flight experiment consisted of two scalar magnetometer sensors and an electronics box hosting three printed circuit boards. The design of the sensors is largely based on previous work (Korth *et al.*, 2016a) and consists of five slices shown in Fig. 1. The first slice [Fig. 1(a)] contains a single-transverse-mode VCSEL diode designed to emit light at 795 nm suitable for the resonant excitation of ^{87}Rb atoms. The VCSEL can be tuned over ±1 nm by adjusting its operating temperature and drive current. To facilitate this tuning, the VCSEL die is mounted on a ceramic substrate heater, along with a chip-based thermistor to measure the laser temperature for thermal control. These parts are wire-bonded on the

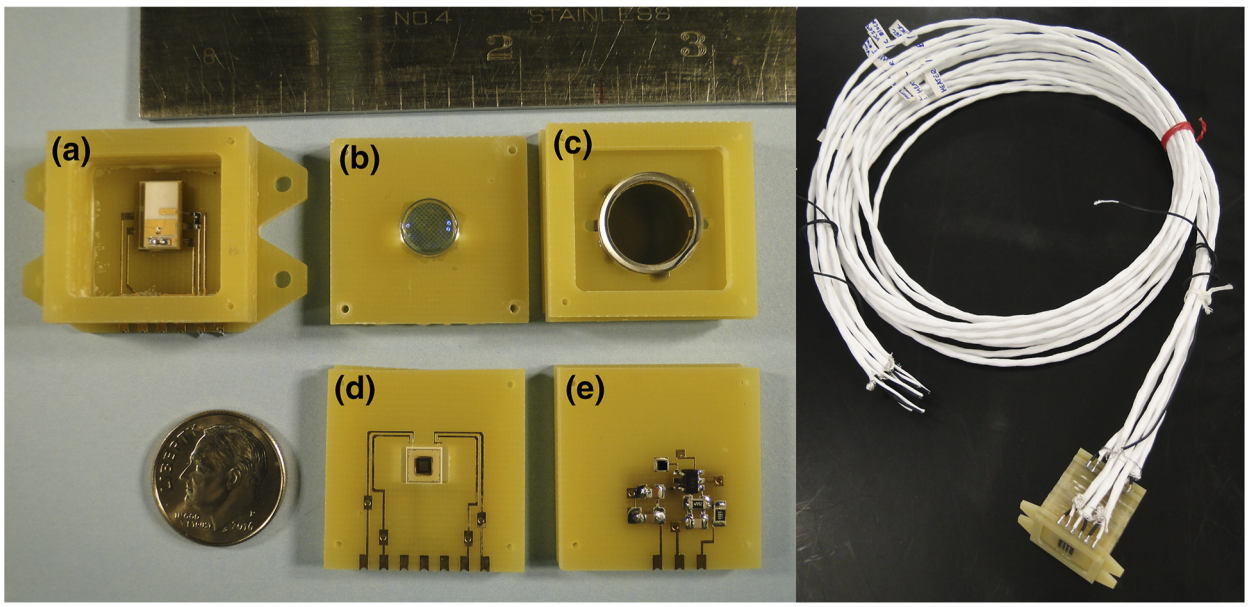

FIG. 1. Magnetometer sensor components (left) showing (a) VCSEL, (b) collimating lens, (c) circular polarizer, (d) ^{87}Rb vapor cell integrated with Helmholtz coils and heaters, and (e) photodiode with a transimpedance amplifier circuit. Assembled sensor with harness (right).

Downloaded from http://pubs.aip.org/aip/rsi/article-pdf/doi/10.1063/5.0135372/16798194/035002_1_online.pdf

© Author(s) 2023

circuit board to conductive traces, which lead to soldering pads at the edge of the board for external connection. The VCSEL emits a linearly polarized, divergent beam of light, which is collimated by a lens contained in the second slice [Fig. 1(b)]. The third slice [Fig. 1(c)] contains a circular polarizer consisting of a linear polarizer and quarter-wave plate, in which axes are aligned at a 45° angle with respect to each other. The fourth slice [Fig. 1(d)] contains a NIST-developed ^{87}Rb vapor cell, which must be heated to ~100 °C to obtain sufficient Rb vapor density. Dimensions of the vapor cell, which also contains nitrogen as a buffer gas, are about $1 \times 1 \times 1$ mm^3. The alkali vapor is excited by an RF magnetic field near the atomic Larmor frequency to drive the atomic spin precession. The functions enabling these requirements have been integrated into a complementary metal–oxide–semiconductor (CMOS) chip and fabricated on a transparent silicon-on-sapphire (SOS) substrate. The vapor cell heater was implemented with a magnetic-field-canceling design using multiple layers of the CMOS chip to provide compensation of magnetic fields generated by current loops within and across layers (Korth *et al.*, 2016b). A set of two such application-specific integrated circuits (ASICs) with an ^{87}Rb vapor cell sandwiched in between was mounted to an alumina substrate for limited thermal isolation. The RF magnetic field is generated by a single-turn coil implemented on each SOS ASIC, and two such coils are mounted in Helmholtz configuration and are uniform across the detection volume to within ~30%. Therefore, the RF field is applied along the propagation axis of the laser beam. A chip thermistor is included for temperature control of the vapor cell. The fifth slice [Fig. 1(e)] contains a photodiode and a transimpedance amplifier (TIA) to amplify the detected photocurrent. In the previous instrument design, the TIA was located in the electronics box to simplify the sensor design. However, this is not ideal because the electronics is not able to compensate for the decreasing signal-to-noise ratio (SNR) associated with a longer harness connecting the sensor to the electronics box in a flight configuration, in which the sensor may be located at the end of a boom. This deficiency was avoided by integrating the TIA directly with the sensor to amplify the signal prior to transmission. The fully assembled sensor with attached harness is shown in Fig. 1 (right).

The magnetometer electronics consists of three printed circuit boards of two unique designs. The first board combines the low-voltage power supply (LVPS) and sensor support electronics board (Fig. 2, left). The LVPS steps the nominal rocket battery voltage of 28 V down to 5 and 3.3 V for use throughout the electronics box. The sensor-support electronics on this board provides a constant current source for the VCSEL diode, drives this component's heater, and measures its temperature for thermal control. It further drives the heater for the vapor cell and controls the vapor temperature. The VCSEL diode heater uses a buck-boost converter programmed with a digital-to-analog converter (DAC) to provide a variable voltage in the range of 0–10 V to the heater. The vapor-cell heater element on the ASIC is a high-resistance heater, and a DAC-programmable boost converter is used to step up the heater voltage to a maximum of 75 V to decrease the current required for heating the cell, thus reducing the contamination magnetic field near the detection volume. Accommodations were included for H-bridge circuits to power the heaters with alternating current (AC), but this functionality was not sufficiently tested and ultimately not used in this rocket experiment. The temperature measurements of the VCSEL and the vapor cell each used a constant current source to drive the thermistor and measure its voltage. The VCSEL diode current source used a DAC-programmable constant current source to allow tuning of the laser's wavelength. All DAC-programmable features used a 12-bit buffered voltage output DAC with an inter-integrated circuit (I^2C) interface. The temperature measurements, along with housekeeping monitoring of the programmable heater voltage and laser current outputs, were taken with a 12-bit successive approximation analog-to-digital converter (ADC) with an I^2C interface. The electronics box included two LVPS slices; on one board, all circuits required to power the flight experiment and operate one of the scalar magnetometer sensors were installed, and on the other board, only those

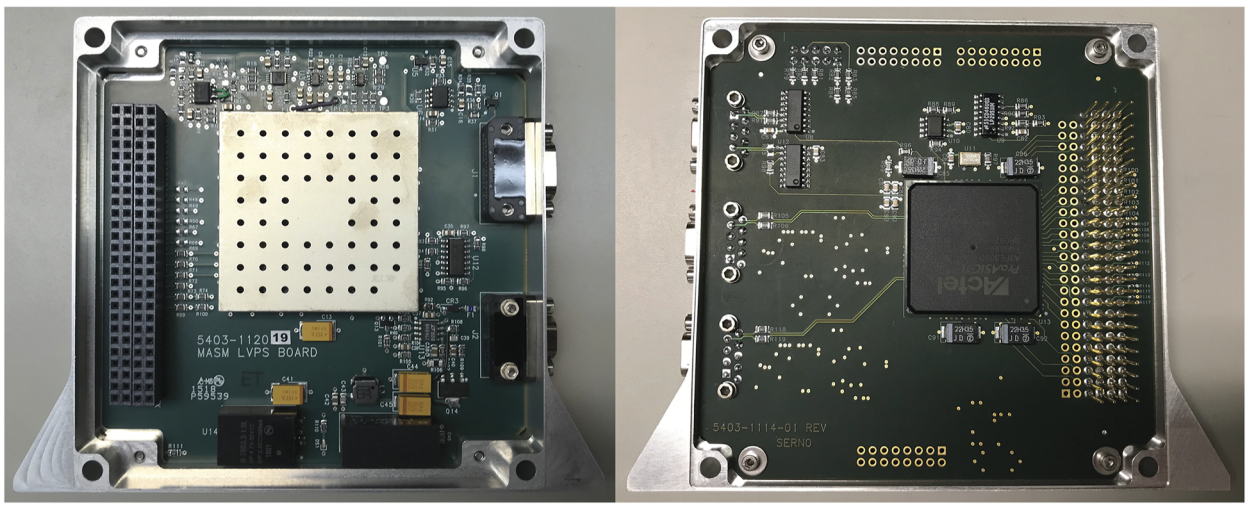

FIG. 2. The magnetometer electronics consists of printed circuit boards for the low-voltage power supply and analog interface (left) and the digital controller (right).

Downloaded from http://pubs.aip.org/aip/rsi/article-pdf/doi/10.1063/5.0135372/16798194/035002_1_online.pdf

© Author(s) 2023

components required for driving the second magnetometer sensor were populated.

The second type of the printed circuit board in the electronics box is a combined two-channel ADC and instrument controller (Fig. 2, right). This board receives the magnetometer signals from both of the scalar sensors, AC-couples them to remove the direct current (DC) component, passes each one through a buffer stage to set the desired DC bias for the ADC, and finally a differential-output amplifier stage before digitizing the signals at 8.33 Megasamples per second (Msps) using separate 14-bit pipelined ADCs. The absolute accuracy and drift of the magnetic field measurement are affected by the onboard oscillator, which provide the clock for the instrument and set the Larmor frequency. The oscillator used to drive the instrument's internal clock is an ECS-3963-500-AU-TR manufactured by ECS, Inc., and has a frequency stability of −/+100 ppm over the full operating ranges of the temperature, input voltage, load, shock, and vibration. For an ambient field of 50 000 nT, the frequency stability implies a potential drift in a measured magnetic field magnitude of about 5 nT. The instrument controller is digitally implemented within a Microsemi ProASIC3E Field Programmable Gate Array (FPGA) operating at 50 MHz and an RS-422 interface to stream data continuously to the rocket's host instrument at a link speed of 115 200 bits per second.

The instrument controller FPGA is responsible for three main functions: maintaining stable temperatures of the laser and vapor cell, processing the magnetometry signals, and sending telemetry. The laser and vapor cell heaters are controlled by proportional-integral control loops based on the respective thermistor feedback. The optimal laser current was determined experimentally prior to launch by monitoring the absorption from the atoms and set to that value by the FPGA. No active wavelength stabilization was implemented during the flight.

To process the magnetometry signals, the FPGA implements a digital lock-in amplifier technique to recover small signals in a noisy environment. The FPGA controls the generation of the RF magnetic field to excite the ^{87}Rb atoms in the vapor cell by driving complementary square waves on output pins connected to the RF Helmholtz coil. The incoming magnetometry signals are sampled at 8.33 Msps by the ADC and read into the FPGA. The signals are then quadrature demodulated relative to the RF magnetic field stimulus output. This produces in-phase (I) and quadrature-phase (Q) signal components relative to the RF stimulus. Using the M_x measurement technique (Bloch, 1946; Bloom, 1962), the RF stimulus frequency is changed until a zero signal is obtained in the I component to yield a phase shift between the applied RF signal and the resonant response of 90°. When achieved, a maximum signal is found in the Q component. The frequency of the RF stimulus at that point is equal to the Larmor frequency corresponding to the ambient magnetic field.

To track dynamically changing magnetic fields, the FPGA implements a sweep-and-track algorithm. First, the RF stimulus is coarsely swept from high to low frequencies, starting at 550 kHz (~78 500 nT), until a global maximum in the Q signal is found. The identified frequency is a coarse approximation of the Larmor frequency and is used to seed the tracking algorithm. This algorithm implements a proportional-integral-derivative (PID) control loop on the RF frequency to servo the I signal to a zero value at the Larmor frequency. The algorithm assumes that the phase change of the I signal as a function of the RF frequency is roughly linear near the zero crossing and sets the PID constants to operate in a nulling mode. Changes in the ambient magnetic field will cause the control loop to similarly change the RF stimulus frequency to remain locked onto the zero crossing in the I signal. The Larmor frequency is approximated by the frequency of this RF signal, which is known, relative to the onboard clock and subject to uncertainties of its oscillator, from the phase accumulation register of the direct digital synthesizer. The FPGA sends the Larmor frequencies measured by both sensors and context telemetry over

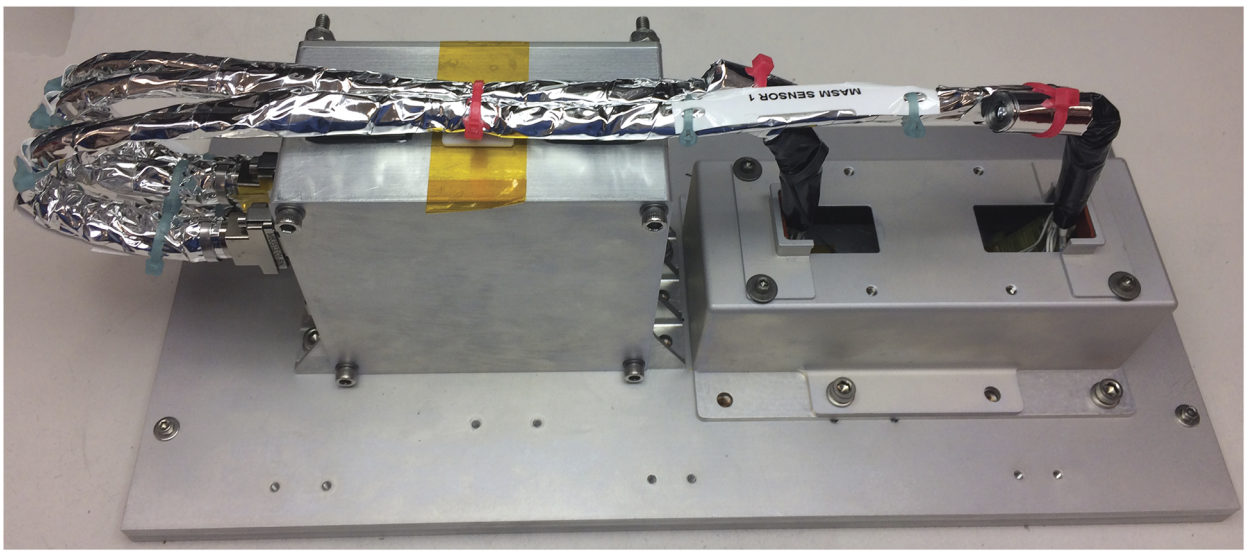

FIG. 3. Photograph of fully assembled flight instrument showing stacked electronics (left) and enclosure housing two sensors (right).

Downloaded from http://pubs.aip.org/aip/rsi/article-pdf/doi/10.1063/5.0135372/16798194/035002_1_online.pdf

© Author(s) 2023

an RS-422 universal asynchronous receiver–transmitter (UART) at a fixed rate of one 16-byte packet per 100 ms. This allows for 10 Hz magnetometer telemetry from both scalar sensors. The FPGA interleaves other telemetry points for context, such as the laser and vapor cell temperature, control loop process variables, digital lock-in amplifier intermediate I and Q values, and the laser diode current.

Upon powering the instrument prior to the rocket launch, a state machine inside the FPGA initiated a startup routine and executed the tracking algorithm. First, the laser current sources were set. Next, the two scalar sensor's laser and vapor cell heater control loops were turned on and allowed to stabilize. To stay under a maximum power draw requirement, the two scalar sensors were staggered one at a time while warming up. Once the sensors reached their operating temperature, the state machine entered an indefinite loop running the frequency sweep routine followed by tracking the magnetic field for 30 s and then repeating this sequence. The periodic maintenance sweep was included in the measurement loop to ensure the system would not lose lock on the magnetic field in the event of any large unexpected magnetic field transients caused by the rocket stages or deployments.

The fully assembled flight instrument is shown in Fig. 3. The three slices of the electronics are contained in the box on the left, and the right-side assembly holds and protects the two magnetic field sensors. The enclosures are fabricated from non-magnetic aluminum. Due to limitations in the accommodation, sensors and electronics had to be mounted in close proximity on the rocket and were, thus, connected by a very short harness. Since the primary purpose of this experiment was the flight demonstration, instrument mass and power resources were designed to match the rocket environment but have not been reduced for resource-constrained environments. As shown, the mass of the instrument excluding the harness and the base plate, which was used for transport only, is about 1 kg, subdivided into 600 g for the electronics and 400 g for the sensor assembly. The instrument power was 5.9 W during warm-up and 3.8 W during nominal operations. The output data rate was limited to 160 bytes per second to match the link speed to the host instrument.

III. MEASUREMENTS

The low-flying TRICE-2 rocket, which carries the MASM, was launched from Andøya, Norway on December 8, 2018 at 08:28 UTC. Figure 4 illustrates the rocket trajectory as functions of latitude and longitude and color-coded by altitude. The rocket released from the rail about 0.5 s after ignition of the first stage. Rocket stage separations occurred 36 and 90 s after launch, and the nose cone was ejected 118 s into the flight followed by payload separation at 120 s. Various deployments occurred between 140 and 160 s after launch. The trajectory passed over the Svalbard islands and crossed through the Earth's northern cusp region reaching a maximum altitude of 756.7 km at 76.8°N latitude and 19.8°E longitude. The universal time at apogee was 08:36:33, and the flight time until impact was just over 17 min.

The time series of the magnetic field magnitude measured by one of the MASM sensors for the duration of operations is shown in the black line in Fig. 5. The instrument was turned on about 5 mins prior to launch allowing the Rb vapor cell to warm up to its operational temperature of ~125 °C. At this time, the TRICE-2 rocket was on the rail, and the MASM recorded the nearly static magnetic field of about 56 000 nT. The recorded magnetic field is the sum of the Earth's field at the launch location and the fields of the launch environment and the rocket, which was not magnetically clean. Following the launch, the time series of the magnetic field magnitude exhibits multiple discontinuities, which coincide with the aforementioned rapid changes in the rocket configuration. After completion of deployment operations about 160 s after launch, the magnetic field varies smoothly as a function of altitude, latitude, and longitude, and it agrees with the International Geophysical Reference Field (IGRF) model (red line) to within a small offset during the science phase of the mission. Unfortunately, the second sensor proved to be unreliable already during the development of the instrument and suffered from intermittent loss of lock on the Larmor frequency, and this issue reoccurred in flight. The data from this sensor are not useful, and we make no attempt to interpret these here.

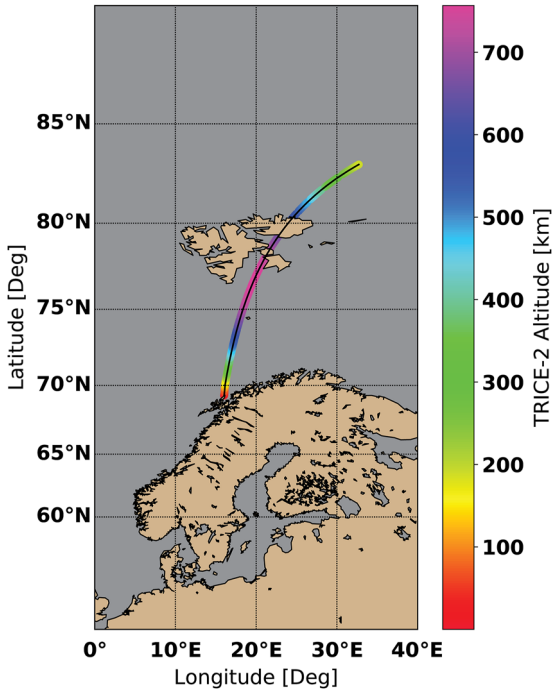

FIG. 4. Trajectory of the TRICE-2 low-flying rocket extends from Andøya, Norway over Svalbard islands and beyond. The altitude is color-coded according to the color bar to the right of the figure and peaked at 750 km just south of Svalbard.

The observations during the science phase of the mission are shown in more detail in Fig. 6. Figure 6 (top) shows the magnetic field magnitude, whereas Fig. 6 (bottom) shows the difference with respect to the IGRF model field depicted in the red line in Fig. 6 (top). The observations are shown in black in Fig. 6 and exhibit two distinct characteristics. First, the data are acquired in 30 s segments with a 10 s gap in between. The gap is the result of the instrument generating invalid data while it is conducting a frequency sweep to reacquire the Larmor frequency. As noted above, this periodic

Downloaded from http://pubs.aip.org/aip/rsi/article-pdf/doi/10.1063/5.0135372/16798194/035002_1_online.pdf

© Author(s) 2023

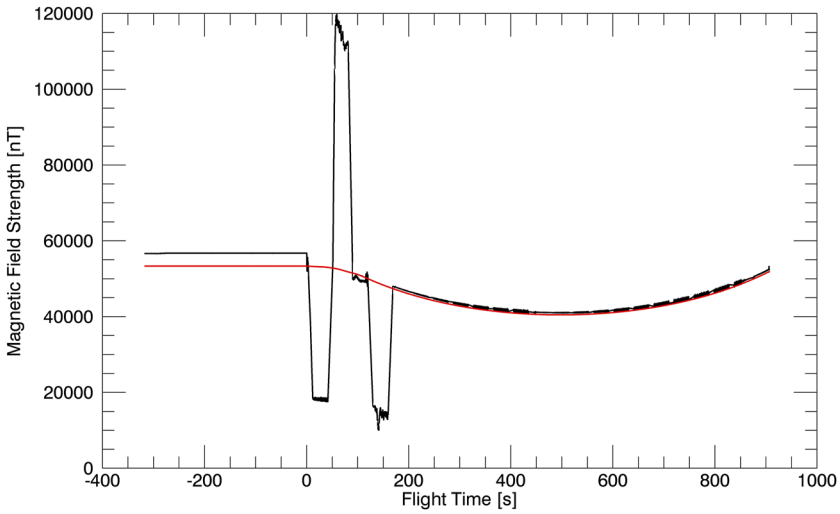

FIG. 5. Time series of the magnetic field magnitude measured by the MASM (black line) and IGRF model at the rocket location (red line).

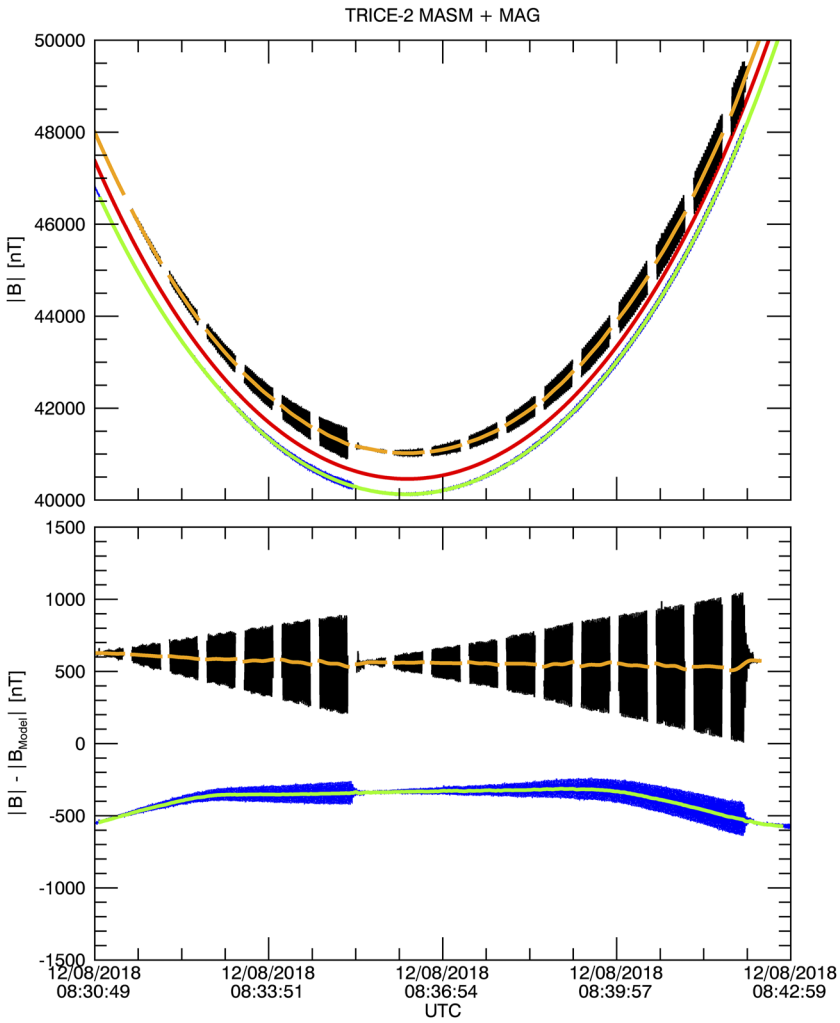

FIG. 6. (Top) High-resolution and spin-averaged observations are shown in black and orange, respectively, for the MASM sensor and in blue and green, respectively, for the rocket's science magnetometer. The IGRF model magnetic field for the corresponding epoch is shown in red. (Bottom) Model residuals (data minus model) for these datasets.

Downloaded from http://pubs.aip.org/aip/rsi/article-pdf/doi/10.1063/5.0135372/16798194/035002_1_online.pdf

© Author(s) 2023

maintenance was implemented to mitigate the risk of the tracking loop losing lock on the Larmor frequency during the flight and not being able to recover from such fault. Second, the variability of the observed magnetic field magnitude increases over time during the ascent of the rocket, then is abruptly reduced near apogee, and increases again on the descending leg of the flight. Closer inspection of the data shows that the measured field magnitude is a function of the rocket spin phase, and this is indicative of the presence of a spacecraft contamination field, which is added or subtracted from the ambient field magnitude depending on vehicle orientation. The variability becomes larger over time as the angle between the rocket's spin axis and the Earth's magnetic field increases and decreases suddenly when an attitude correction maneuver aligns the rocket with the ambient magnetic field direction just before apogee. Assuming that spacecraft internal magnetic fields are fixed in amplitude and direction in the frame of the rocket, removal of the contamination field can be pursued by piecewise fitting a sinusoid with amplitude linearly increasing over time and then inferring the ambient field from the offset of the fit wave. Such an attempt to recover the ambient field was successful to first order as represented in orange lines in Fig. 6 but is less successful at the boundary of the data packets where the fit becomes less reliable. Finally, the magnetic field data from the mission's science fluxgate magnetometer are shown in blue and are overlaid by the spin-averaged values shown in green. The science magnetometer is mounted at a different location, and the data, therefore, exhibit an offset with respect to the IGRF model, which differs from that of the MASM. The differences in the magnetic field measured by both instruments with respect to the model field are in the range expected for a flight program without focus on magnetic cleanliness. Similar to the MASM data, the spin data (blue trace) show an increase in variability over time and a sudden decrease in variability near apogee. In contrast to the MASM measurements, the deviation between the spin-averaged magnetic field magnitudes registered by the science instrument and the IGRF model field is not constant in time but shows systematic drifts of about 200 nT at the beginning and end of the flight. The cause of this drift is unknown, and its investigation is beyond the scope of this paper.

IV. POST-FLIGHT LABORATORY CHARACTERIZATION

The development schedule for the rocket experiment did not include sufficient time for performance characterization prior to launch. To distinguish instrumental fluctuations in the measurement from environmental effects, a limited performance characterization was performed post-launch using the engineering model instrument. The focus of this assessment was to establish and improve the temporal stability of the measurement and to determine the measurement offset resulting from electronic phase shifts. These laboratory experiments, carried out with a single engineering model sensor in a controlled magnetic field generated inside a shielded environment, are described in this section.

A. Measurement stability

A stable reading of the magnetic field magnitude requires that the magnetic resonance at the Larmor frequency be identified precisely. The measurement stability of the instrument was determined by operation in a static magnetic field applied within the shielded environment. For this characterization, samples were acquired at a rate of 125 samples per second over a duration of 8 s. Two such time series acquired in an approximate field of 9320 nT are depicted in Fig. 7, and a 1–σ standard deviation of 1.43 nT was computed from these data.

The ability to determine precisely the Larmor frequency is directly linked to the width and shape of the resonance line, which depend on the properties of the vapor cell, the amplitude of the RF signal stimulating the atomic resonance, and the intensity of the laser light optically pumping the rubidium atoms. Modifications of the vapor cell design are beyond the scope of this paper, and properties of the vapor cell are not further examined here. Instead, we are focused on assessing the tuning of the electronic signals to optimize the atomic resonance feature.

Nominally, the flight electronics sample and process the resonance curve onboard and only report the Larmor frequency as the frequency at which the phase of the Larmor precession with respect to the drive frequency amounts to 90°. To determine and optimize the tuning of the magnetometer, the electronics were modified to capture the raw sensor output to generate an IQ-magnitude resonance curve and determine its shape and identify any artifacts generated by the flight software. Examples of resonance curves recovered from the raw samples are shown in Fig. 8. The blue line resembles the resonance curve associated with the RF field amplitude of about 760 nT, as implemented in the flight experiment. This signal is both broad and double peaked, which is indicative of the RF power being too strong, and these features reduce the sensitivity of the atomic phase shift to changes in RF frequency or magnetic field. This in turn reduces the field sensitivity of the magnetometer. To improve the frequency measurement, the amplitude of the RF stimulation was lowered to ~200 nT using a resistor in series with the RF excitation coil (the orange dashed line in Fig. 8). The resonance curves have been normalized for direct comparison of the signal shapes. Reducing the RF power to about one-fourth of its original value eliminated the double peak and yielded a narrower resonance curve with a better defined center peak. Therefore, the decreased RF drive amplitude is more appropriate for a future flight instrument. Using this configuration, the sensitivity of the resonance

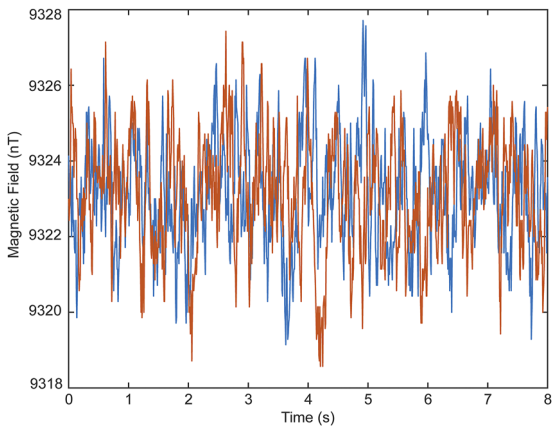

FIG. 7. Two sample time series of 8 s duration shown in distinct colors. The data were acquired at a rate of 125 samples per second.

Downloaded from http://pubs.aip.org/aip/rsi/article-pdf/doi/10.1063/5.0135372/16798194/035002_1_online.pdf

© Author(s) 2023

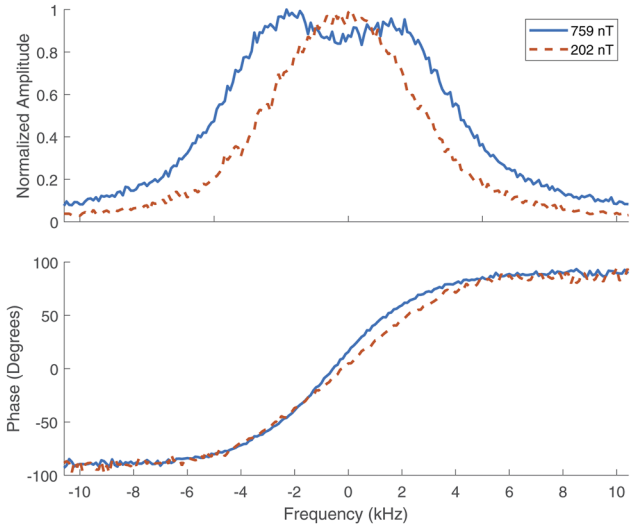

FIG. 8. Dependence of resonance amplitude and phase on RF drive frequency for two RF signal amplitudes. The signal's amplitude is normalized to the peak response, and the phase has been shifted by 90°.

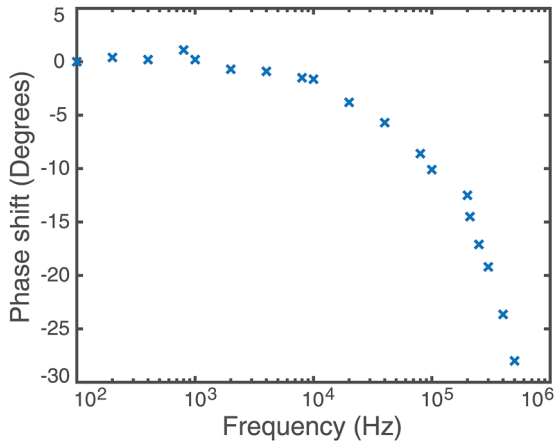

FIG. 9. Dependence of the TIA phase shift on frequency.

line shape to the laser intensity was tested by reducing the laser output power by 50%. This experiment showed no observable change in the resonance curves, implying that the width of the resonance is not very sensitive to the intensity of the optical pumping at the optical intensities used during flight. Assuming that the effect of the laser intensity on linewidth is similar for higher RF power, the laser current of the flight instrument was reasonably well-tuned. It should be noted that the lock-in detection that generated the phase curve in Fig. 8 was implemented without any adjustment of the relative phase between the reference signal and the digitized photodiode output. Therefore, any phase shifts in the electronics would be expected to cause an error in the magnetometer output as discussed below.

B. Instrumental phase shift

Atomic magnetometers based on the M_x mode measure the Larmor frequency as a 90° phase shift between the RF stimulation signal, which is applied to the vapor cell, and the optically registered resonant response, and their accuracy is, therefore, sensitive to phase shifts inherent to the electronics. For an accurate measurement, it is thus important that the instrument electronics does not affect the phase of the measured signal in an unknown way. We measured the phase shift to correct the flight data and determined its cause for future improvement of the instrument. We characterized the electronic phase shift caused by a transimpedance amplifier (TIA) that amplifies the photocurrent to increase the signal-to-noise ratio, thus improving the signal processing within the instrument.

Measurements of the phase shift are shown in Fig. 9 and vary between −16° and −20° for the magnetic field range of the TRICE-2 mission (40 000–50 000 nT). The phase shift, φ, can be converted into a magnetic field error using the phase relationship for an ideal M_x magnetometer,

$$\varphi = \arctan\left(\frac{\omega_{rf} - \omega_m}{\gamma}\right), \tag{1}$$

where ω_{rf} is the RF frequency, ω_m is the true frequency, and γ is the linewidth estimated to be 7000 Hz (cf. Fig. 8). The resulting magnetic field error, shown in Fig. 10, linearly depends on the magnetic field magnitude and ranges between −270 and −330 nT for this instrument and mission. Thus, the phase shift accounts for about half of the observed magnetic field offset depicted in Fig. 6, where this correction has not been applied. For future flight instruments, a phase correction can be achieved by calibrating the electronics on the ground prior to launch. An alternative solution to the problem is to use the M_z measurement technique (Bloom, 1962), which is manifested in an amplitude variation of the resonant response and is not affected by electronic phase shifts. An M_z-mode magnetometer has since been implemented and is currently under test.

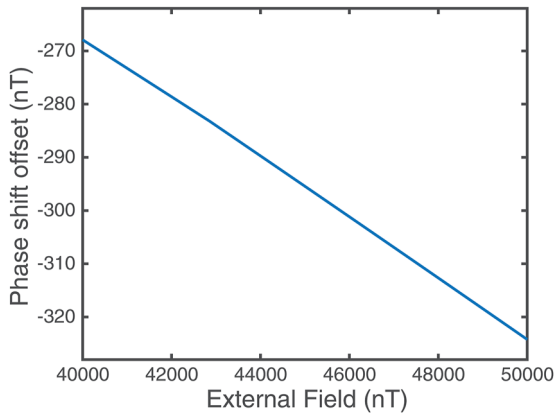

FIG. 10. Dependence of magnetic field error resulting from the TIA phase shift on magnetic field magnitude.

Downloaded from http://pubs.aip.org/aip/rsi/article-pdf/doi/10.1063/5.0135372/16798194/035002_1_online.pdf

© Author(s) 2023

V. DISCUSSION

The primary purpose of adding the MASM as a ride-along experiment to the TRICE-2 low-flying rocket was to demonstrate the flight qualification of the instrument and thereby increase the instrument's Technology Readiness Level (TRL). To qualify for flight, the instrument must be capable of withstanding the physical stresses during launch and flight, operating in the rocket or spacecraft thermal environment, and acquiring data of scientific quality throughout the mission. The fact that valid science data were obtained throughout the science campaign implies that the instrument is fundamentally robust to the mechanical loads and thermal environments encountered within this rocket campaign and that the environmental success criteria have thus been. In this section, the engineering and scientific success criteria are discussed in additional detail.

From the engineering perspective, successful operation requires the following conditions for the hardware. First, the Rb vapor cell must maintain its temperature independent of the rocket's thermal environment to ensure a sufficient vapor density. We found that the heater for the vapor cell performed nominally and maintained a near constant temperature of 124.2 °C as measured by the cell thermistor, and departures from the nominal temperature were less than 2 °C during the launch phase and about 0.1 °C during the science phase of the mission. Second, the VCSEL temperature must be controlled precisely to preserve a wavelength of 794.98 nm and ensure efficient optical pumping at this magnetically sensitive absorption line. The instrument's housekeeping data showed that the laser temperature was maintained to within <0.1 °C of the nominal value of 47.1 °C during the science phase. This corresponds to a wavelength stability of below 0.01 nm (5 GHz). This is consistent with the fact that the magnetometer operated continuously; a laser frequency detuning by more than a few GHz from the atomic transition would have caused a loss of signal and corresponding loss of Larmor frequency lock. During the launch phase, the laser temperature varied somewhat more than 0.5 °C, and various large steps in the magnetic field recorded early after launch, coinciding with the separation of the rocket stages, could be artifacts of an incorrectly tuned laser. Finally, the control loop, which servos the sensor RF field to the Larmor frequency and thereby provides a measure of the magnetic field, must track the field magnitude continuously and not lose lock on the Larmor frequency. The downlinked telemetry shows that the data are indeed continuous with exception of the gaps associated with commanded frequency sweeps. While these frequency sweeps do not appear to be necessary for smooth changes in the magnetic field magnitude observed during the science phase, they were critical during the launch phase when the magnetic field showed large discontinuities associated with the stage separations and/or the instrument performance was perhaps degraded due to rapid changes in the thermal environment. Overall, the complete acquisition of valid data demonstrates that the instrument performed extremely reliably from the engineering perspective.

The science performance of the instrument was assessed by comparison with both the IGRF model field and the data acquired by the campaign's science magnetometer and in the context of the effects of contamination fields attributed to the rocket. The instrument performance is assessed by comparison with both the IGRF model field and the data acquired by the campaign's science magnetometer. Prior to launch, the MASM observations exceeded the magnetic field magnitude predicted by the IGRF model by about 4000 nT (cf. Fig. 5). While the model can only estimate the magnetic field at a given location, the discrepancy with respect to the observations is much larger than typical and cannot be attributed to an uncertainty in the model. The difference likely results from magnetized components within the rocket itself and at the launch site. In addition, electric current loops within the sensor may generate small contributions to the measured magnetic field. Following the launch, discontinuities of many tens of thousands of nT are observed at times of stage separation and other changes in the rocket configuration. While changes in spacecraft magnetic field contributions are expected in association with these events and result in discontinuities in the measured magnetic field magnitude, the observed shifts are unexpectedly large. During this time, the science magnetometer registers instantaneous spikes in the magnetic field with amplitudes ranging from tens of thousands to 100 000 nT, which may be the result of electromagnetic interference associated with stage separations. Based on these observations, the step-like changes in the magnetic field observed by the MASM may be due to limitations in the instruments tracking algorithm. The algorithm requires that the maximum allowed change in the ambient magnetic field between two successive measurements does not exceed the linewidth of the magnetic resonance. Figure 8 shows that the full width at half maximum (FWHM) of the resonance is of the order 8000 Hz, or 1000 nT, and corresponds to the maximum allowed rate of change in the magnetic field over a period of 0.1 s given the measurement sampling rate of 10 Hz. The fact that the science magnetometer registers discontinuities that are 10–100 times larger than the MASM's measurement capability suggests that the instrument temporarily lost lock on the Larmor frequency and reported an incorrect magnetic field magnitude during this time. The instrument recovered automatically once the payload was fully configured for the science phase of the mission.

Entering the science phase about 200 s after launch, the spin-averaged magnetic field measurements vary smoothly and compare favorably with the IGRF to within an average offset of 550–600 nT. The offset is roughly stable in time and plausibly attributed to rocket magnetic fields. However, it cannot be ruled out that a phase shift introduced by electronics provides an offset as well. This instrumental characteristic can generally be measured and corrected but such calibration was not performed due to a lack of time. The need for such calibration can also be avoided entirely by using the M_z technique (Bloom, 1962), which measures the amplitude of the modulation signal rather than its phase, to measure the magnetic field.

Since the atomic magnetometer is a scalar sensor, an oscillatory component observed at the spin period indicates that the rocket magnetic field has a component parallel or anti-parallel to the ambient magnetic field direction, which amplifies or reduces the Earth's magnetic field magnitude depending on the spin phase. The amplitude of this oscillation is time-dependent because the rocket cone angle, i.e., the angle between the rocket spin axis and the local magnetic field direction, increases over time as the projection of the contamination field vector onto the ambient field direction becomes larger. The cone-angle dependence is most readily observed just before apogee when the payload spin axis was actively re-aligned with the ambient field direction to rapidly reduce the contamination field component parallel to the ambient field and thus the amplitude

Downloaded from http://pubs.aip.org/aip/rsi/article-pdf/doi/10.1063/5.0135372/16798194/035002_1_online.pdf

© Author(s) 2023

of the oscillation signal. The oscillating field and dependence on the cone angle are also observed qualitatively by the science magnetometer. The amplitude of the oscillation is reduced in this instrument's data because the sensor is mounted on a mast further away from magnetized rocket and/or payload components.

The spin-period signal is difficult to correct for in part because the signal is under-sampled and because the spin period varies slightly during the flight. A correction was attempted by subtracting from the data a piecewise fit of a sine wave with linearly increasing amplitude to the 30 s data packets. While this markedly reduced the variability in the observations by about an order of magnitude, a residual signal with 50 nT amplitude remained. The frequency content of the residual signal is dominated by the spin period and its harmonics and implies that these residuals do not represent the noise of the instrument itself. The offset of this fit is depicted by the orange trace in Fig. 6(b). As noted in Sec. III, the sinusoidal fits yield less accurate results near the boundaries of the data packets. Nevertheless, the processed data suggest that the offset decreases during the first half of the flight from about 600 nT to about 550 nT, while it appears more stable during the latter half. The offset drift is not correlated with the rocket altitude or the magnetic field magnitude, and the laser and vapor cell temperatures are stable for the duration of the science phase. We hypothesize that the effect results from warming of the electronics but the housekeeping data are insufficient to identify definitively the root cause.

VI. SUMMARY

In conclusion, we have demonstrated the operation of an atomic magnetometer based on a miniature rubidium vapor cell in a sounding rocket environment. The instrument fully functioned throughout the flight, and deviations of the measured magnetic field from model predictions were explained by correctable instrumental offsets and spacecraft magnetic fields. We did not encounter any unanticipated operational anomalies inflight and did not identify any noise or artifacts in the data beyond those described in this paper. For future instruments, the contribution to the offset from phase shifts in the electronics needs to be measured, and the root cause of the offset drift needs to be confirmed. We have developed this instrument to provide highly accurate magnetic field measurements for scientific missions in space, where this instrument can also serve as a reference to calibrate in flight other vector magnetometers, such as fluxgate magnetometers, which may drift over time, especially during missions with long cruise durations. The successful flight operation provides confidence that the instrument has great potential to perform well in future space flight mission.

ACKNOWLEDGMENTS

We thank the Principal Investigator of the TRICE-2 mission, Dr. Craig Kletzing, for the opportunity and his support to qualify this novel instrument for spaceflight. We thank Dr. Svenja Knappe for fabricating the vapor cell used in the experiment. This paper was supported by the National Aeronautics and Space Administration (Grant Agreement No. NNX16AG20G) through the Science Mission Directorate.

AUTHOR DECLARATIONS

Conflict of Interest

The authors have no conflicts to disclose.

Author Contributions

Haje Korth: Conceptualization (equal); Data curation (equal); Formal analysis (equal); Funding acquisition (lead); Investigation (lead); Methodology (equal); Project administration (lead); Resources (equal); Software (equal); Supervision (lead); Validation (equal); Visualization (equal); Writing – original draft (lead). **John E. Kitching**: Conceptualization (equal); Methodology (equal); Resources (equal). **John W. Bonnell**: Data curation (equal); Resources (equal). **Brian A. Bryce**: Formal analysis (equal); Investigation (equal); Validation (equal); Visualization (equal). **George B. Clark**: Formal analysis (equal); Investigation (equal); Project administration (equal). **Weston K. Edens**: Conceptualization (equal); Data curation (equal); Methodology (equal); Software (equal). **Christopher B. Gardner**: Conceptualization (equal); Data curation (equal); Methodology (equal); Project administration (equal). **William Rachelson**: Data curation (equal). **Amanda Slagle**: Data curation (equal).

DATA AVAILABILITY

The data that support the findings of this study are openly available in zenodo.org at http://doi.org/10.5281/zenodo.7158204.

REFERENCES

Acuña, M. H., "Space-based magnetometers," Rev. Sci. Instrum. **73**, 3717 (2002).

Bloch, F., "Nuclear induction," Phys. Rev. **70**, 460–474 (1946).

Bloom, A. L., "Principles of operation of the rubidium vapor magnetometer," Appl. Opt. **1**(1), 61 (1962).

Budker, D. and Jackson Kimball, D. F., *Optical Magnetometry*, (Cambridge University Press, 2013).

Kitching, J., "Chip-scale atomic devices," Appl. Phys. Rev. **5**, 031302 (2018).

Knappe, S., Shah, V., Schwindt, P. D. D., Hollberg, L., Kitching, J., Liew, L.-A., and Moreland, J., "A microfabricated atomic clock," Appl. Phys. Lett. **85**, 1460 (2004).

Korth, H., Strohbehn, K., Tejada, F., Andreou, A. G., Kitching, J., Knappe, S., Lehtonen, S. J., London, S. M., and Kafel, M., "Miniature atomic scalar magnetometer for space based on the rubidium isotope ^{87}Rb," J. Geophys. Res.: Space Phys. **121**, 7870, https://doi.org/10.1002/2016ja022389 (2016a).

Korth, H., Strohbehn, K., Tejada, F., and Andreou, A. G., "Gas cell semiconductor chip assembly," US Patent 9274186 (March 1, 2016b).

Liew, L.-A., Knappe, S., Moreland, J., Robinson, H., Hollberg, L., and Kitching, J., "Microfabricated alkali atom vapor cells," Appl. Phys. Lett. **84**(14), 2694 (2004).

Liew, L.-A., Moreland, J., and Gerginov, V., "Wafer-level filling of microfabricated atomic vapor cells based on thin-film deposition and photolysis of cesium azide," Appl. Phys. Lett. **90**(11), 114106 (2007).

Mescher, M. J., Lutwak, R., and Varghese, M., "An ultra-low-power physics package for a chip-scale atomic clock," in *The 13th International Conference on Solid-State Sensors, Actuators and Microsystems, 2005. Digest of Technical Papers. TRANSDUCERS '05* (IEEE, 2005), Vol. 1, pp. 311–316.

Downloaded from http://pubs.aip.org/aip/rsi/article-pdf/doi/10.1063/5.0135372/16798194/035002_1_online.pdf

© Author(s) 2023

Mhaskar, R., Knappe, S., and Kitching, J., "A low-power, high-sensitivity micromachined optical magnetometer," Appl. Phys. Lett. **101**, 241105 (2012).

Ness, N. F., L Skillman, T., Heppner, J. P., and Scearce, C. S., "Measurements by a rocket-borne rubidium vapor magnetometer," J. Geophys. Res. **66**(8), 2549, https://doi.org/10.1029/JZ066i008p02509 (1961).

Schwindt, P. D. D., Knappe, S., Shah, V., Hollberg, L., Kitching, J., Liew, L.-A., and Moreland, J., "Chip-scale atomic magnetometer," Appl. Phys. Lett. **85**(26), 6409 (2004).

Schwindt, P. D. D., Lindseth, B., Knappe, S., Shah, V., Kitching, J., and Liew, L.-A., "Chip-scale atomic magnetometer with improved sensitivity by use of the M_x technique," Appl. Phys. Lett. **90**(8), 081102 (2007).

Downloaded from http://pubs.aip.org/aip/rsi/article-pdf/doi/10.1063/5.0135372/16798194/035002_1_online.pdf

© Author(s) 2023